J Mater Sci (2006) 41:7785–7797
DOI 10.1007/s10853-006-0624-4

Diffusion reactions at Al–$MgAl_2O_4$ interfaces—and the effect of applied electric fields

Y. Yu · J. Mark · F. Ernst · T. Wagner · R. Raj

Received: 29 March 2006 / Accepted: 26 June 2006 / Published online: 24 October 2006

Abstract Diffusion reactions between $MgAl_2O_4$ (spinel) single-crystal substrates and epitaxial Al layers were studied by transmission electron microscopy (TEM) imaging and analysis. The specimens were annealed for 10 and 20 h at 893 K in ultra-high vacuum. In addition to plain annealing, we annealed while applying electric fields across the $MgAl_2O_4$, either oriented in the direction from the Al to the $MgAl_2O_4$ or opposite. TEM revealed that plain annealing enables a diffusion reaction during which the $MgAl_2O_4$ region adjacent to the interface becomes depleted of Mg and enriched in Al. An electric field oriented in the direction from Al to $MgAl_2O_4$ accelerates the reaction, while a field in the opposite direction retards it. The observations agree with an ion exchange mechanism proposed earlier, implying transport of Mg into the metal. However, Mg transport into the opposite direction also contributes to the reaction. The experimental observations demonstrate that annealing in electric fields can effectively control interface microstructures and properties.

Y. Yu · J. Mark · F. Ernst (✉)
Department of Materials Science and Engineering,
Case Western Reserve University, 10900 Euclid Avenue,
Cleveland, OH 44106-7204, USA
e-mail: frank.ernst@case.edu

T. Wagner
Max-Planck-Institut für Metallforschung,
Heisenbergstraße 5, 70569 Stuttgart, Germany

R. Raj
Engineering Center, University of Colorado Boulder,
Colorado 80309, USA

Introduction

Recent work [1] on spinel ($MgO \cdot 1.25Al_2O_3$) nanoparticles dispersed in Al (aluminum) suggested an *ion exchange* reaction at the Al–spinel interface, characterized by cross-diffusion of (i) Mg^{2+} (magnesium) ions from Mg positions in the spinel into the Al metal and (ii) Al atoms from the Al metal into Mg positions of the spinel. The Mg positions of spinel require a charge of (2+), but the incorporated Al ions carry the charge (3+) [2]. Accordingly, a one-to-one exchange of Al for Mg generates charged point defects [1, 3]

$$Mg_{Mg}^{\times} + Al(ss) \longrightarrow Mg(ss) + Al_{Mg}^{\bullet} + e', \tag{1}$$

where ''ss'' refers to the solid solution of Mg in Al on the metal side. The condition of charge neutrality in ionic crystals requires this reaction to be accompanied by further reactions involving charged point defects in the $MgAl_2O_4$, such as [1].

$$Mg_{Mg}^{\times} + e' \longrightarrow Mg'_{Al} \tag{2}$$

or

$$Al_{Mg}^{\bullet} + e' \longrightarrow Al_{Al}^{\times}. \tag{3}$$

As a result of (1), the spinel becomes enriched in Al^{3+} ions (relative to Mg^{2+} ions), while the outward diffusing Mg forms a solid solution and/or intermetallic compounds with the Al matrix. Since the above reactions alter the population of charged point defects in the oxide, such ion exchange should impact the adhesion between the metal and the oxide. Investigating this possibility may throw new light on the fundamental

question about the possible bonding mechanism between metals and ceramics, which is of great importance for fundamental research and many technical applications (e.g. joining of functional ceramics to metals, packaging of microelectronic devices, oxide dispersion-strengthened alloys, or protective oxide coatings on metals) [4–9]. The correlation between metal–oxide adhesion and the distribution of electric charges in the oxide constitutes the basis for a quantitative theory of metal–oxide adhesion, known as the ''image charge'' model [10–13]: According to the laws of electrostatics, positioning a charge q at a distance z_0 in front of a metal surface causes quasi-free charges in the metal to re-arrange and create a charge density distribution

$$\rho[r] = -q \cdot \frac{z_0}{2\pi(z_0^2 + r^2)^{3/2}}, \quad (4)$$

where r is the lateral distance from q (parallel to the metal surface). The corresponding electric field is the same as if an ''image charge'' of opposite sign, $-q$, were placed at $(-z_0, r = 0)$ behind the metal surface. Consequently, q is *attracted* to the metal. At metal–oxide interfaces, correspondingly, the ions in the oxide generate image charges which attract them towards the metal. The corresponding Coulomb forces should account—at least partly—for the adhesion between metals and oxides (or, more general, ionic ceramics) [14].

As a continuum theory, the original image charge model fails at small distances—directly at a metal–oxide interface—because it does not correctly account for the atomistic structure of the metal and the band structure of its electrons $(z_0, r \to 0 \Rightarrow \rho \to -\infty)$. Later extensions of the model, however, correctly account for the discreteness of the metal lattice [14, 15] and lead to realistic predictions of interface structures [16–18]. For the Al–$MgAl_2O_4$, in particular, recent atomistic simulations [19], based on the DFT (density functional theory) and supported by a highly precise assessment of the Al–$MgAl_2O_4$ interface structure by digital processing of high-resolution transmission electron microscopy (HRTEM) images [20], have revealed that for a structurally perfect oxide, the contribution of image charge interaction to the bonding is relatively weak. However, the presence of charged point defects may result in a much stronger contribution of image charge interaction. Therefore, an ion exchange reaction that builds up a space charge layer at the Al–$MgAl_2O_4$ interface should have profound consequences on the adhesion and the related mechanical properties of these interfaces. On the other hand, re-distribution of electrical charge at a metal–oxide interface can have substantial impact on the kinetics of the diffusion reactions that take place at the interface [21, 22]. Considering the technical importance of metal–oxide interfaces, it is therefore important to understand the diffusion reaction between Al and $MgAl_2O_4$ at a fundamental, quantitative level.

In this publication, we report annealing experiments carried out on Al–$MgAl_2O_4$ interfaces prepared by molecular beam epitaxy (MBE). Utilizing advanced methods of transmission electron microscopy (TEM), we have studied the interface structure and the corresponding spatial distribution of atomic species before and after annealing with high spatial resolution. The results of this work lead to a new and much more detailed understanding of the diffusion reaction at the Al–$MgAl_2O_4$ interface and the microstructural changes that go along with this reaction. Moreover, we demonstrate that the spatial distribution of ions and the microstructure of the Al–$MgAl_2O_4$ interface can be substantially manipulated by the application of (static) electric fields during annealing. Our observations suggest that diffusion reactions under applied electric fields can sensitively alter the strength of interfacial bonding and—consequently—can be used to control the mechanical properties of Al–$MgAl_2O_4$ and related metal–oxide interfaces.

Experimental

Fabrication of Al–$MgAl_2O_4$ interfaces

Planar Al–$MgAl_2O_4$ interfaces, particularly suitable for microcharacterization by TEM, were fabricated by depositing Al onto (001)-oriented substrates of stoichiometric $MgAl_2O_4$ (MTI Corp., Richmond, CA). The substrates had a cross-section of 10×10 mm^2, a thickness of 0.50 mm, and the (001) growth surface was polished by the supplier to a roughness of less than 0.5 nm. After the deposition of Al, the thickness of the substrates was reduced to 0.25 mm by SiC abrasive papers (P1200 and P4000) to reduce the voltage required to obtain a sufficiently high electric field across the spinel during annealing under applied electric fields (Sect. ''Annealing experiments'').

For growing Al thin films on these substrates with high structural quality, we employed MBE, which operates in ultra-high vacuum (UHV, $\approx 5 \times 10^{-9}$ Pa) [23]. The Al to be deposited was evaporated from a source of highly pure Al by electron beam heating. The substrates were first cleaned by in situ sputtering with Ar^+ ions. The effectiveness of the cleaning procedure was verified by in situ Auger electron spectrometry.

Subsequently, the substrates were annealed for 1 h at 1273 K. After this preparation, epitaxial Al layers were deposited at a growth rate below ≈0.1 nm/s. In prior work [19, 24, 25], we had adjusted the substrate temperature between 673 and 873 K and had found that the Al initially grows in the form of epitaxial islands, which persist at least until the amount of deposited Al is equivalent to that of a 200 nm thick continuous layer. In the present study, in contrast, we kept the substrate temperature at room temperature to avoid the onset of diffusion reactions during layer growth and grew the Al layers to a final thickness of 500 nm. Under these conditions we obtained continuous Al layers.

Annealing experiments

Al layers grown on $MgAl_2O_4$ by MBE were annealed in a UHV chamber for different times at 893 K (620 °C), ≈40 K below the melting point of Al (933 K). The temperature was adjusted by resistive heating of a quartz furnace, around which we wound a nichrome wire, and controlled by a thermocouple in direct contact with the $MgAl_2O_4$ substrate.

In addition to plain annealing experiments, we annealed Al–$MgAl_2O_4$ specimens while applying a constant voltage U_a across the $MgAl_2O_4$, generating an electric field E_a. Figure 1 schematically depicts the assembly we designed for carrying out these experiments on Al–$MgAl_2O_4$ interfaces fabricated by MBE. In this construction, electrical contact between the voltage supply and the specimen was established by sandwiching the specimen between two flexible Al sheet electrodes, which in turn were sandwiched between rigid glass–ceramic plates. The assembly also included a thermocouple, sensing the annealing temperature T_a directly at the specimen. Intimate mechanical and electrical contact between all components was established by two screws, pressing the layers of the sandwich together when tightened. With this method, we obtained reproducible results for the microstructure of the Al–$MgAl_2O_4$ interface—we did not observe significant variations in the microstructure of TEM specimens from different regions of the sandwiches. By means of electrical feed-throughs, the electrodes and the thermocouple were connected to the DC power supply and a temperature controller, respectively, outside of the vacuum chamber. In order to limit the external voltage required for obtaining the desired electric field strength across the (insulating) $MgAl_2O_4$ substrate, the thickness was reduced to 250 μm by mechanical polishing.

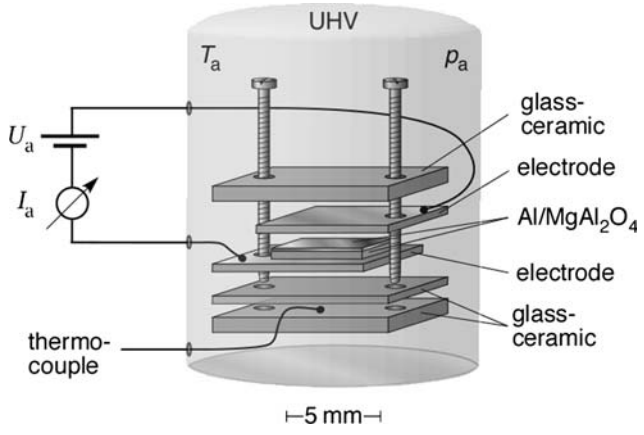

Fig. 1 Schematic illustration of the setup we used for annealing of Al–$MgAl_2O_4$ interfaces in UHV and under an applied electric field. The polarity of the voltage supply shown here corresponds to $U_a > 0$

During all annealing experiments with an applied electric field, the DC power supply (Hewlett-Packard Company, 6209B) maintained a constant voltage (electric potential difference)

$$U_a := \phi_{Al} - \phi_b \tag{5}$$

across the $MgAl_2O_4$ layer, where ϕ_{Al} denotes the electric potential of the MBE-grown Al layer and ϕ_b the potential of the back-electrode. With this definition, $U_a > 0$ corresponds to positive bias of the metal, $U_a < 0$ to negative bias of the metal versus the oxide.

The applied voltage U_a was adjusted to generate an average electric field strength of $|\boldsymbol{E}_a| = 5 \times 10^5$ V/m across the thickness of the spinel substrate. For the chosen thickness of 250 μm for the $MgAl_2O_4$ substrate, this corresponds to a voltage of $U_a = \pm 125$ V between the upper and lower substrate surface. The electric current through the circuit was continuously monitored and recorded by an ampere meter.

Microcharacterization

To study the structure of the Al–$MgAl_2O_4$ interfaces and characterize the spatial distribution of atomic species after different treatments, we employed TEM, including conventional TEM (CTEM), selected-area electron diffraction (SAD), high-resolution TEM (HRTEM), scanning TEM (STEM) with a high-angle annular dark-field (HAADF) detector, elemental mapping by electron-spectroscopic imaging (ESI), and X-ray energy dispersive spectroscopy (XEDS).

For these investigations, we used a Tecnai F30 S-TWIN (FEI, Eindhoven, Netherlands), a 300 kV field-emission gun energy-filtering high-resolution analytical scanning transmission electron microscope.

Operated under optimum conditions for conventional HRTEM, the information resolution limit of this instrument is 0.14 nm. For energy-filtering TEM, the instrument is equipped with a post-column imaging energy filter (''GIF 2001,'' Gatan), retrofitted with a $2\,k \times 2\,k$ charge-coupled device (CCD) camera. For the present work, we applied the ''three-window method'' [26] of electron-spectroscopic imaging for elemental mapping of Al, Mg, and oxygen. Table 1 indicates the settings we have employed for these experiments. For acquiring Mg and Al maps, we used L-edges rather than K-edges because the signals of the latter are so weak that acceptable signal-to-noise ratios require excessive electron doses, likely to introduce beam-damage- and drift-related artifacts. The Mg-L edge, however, is close to the plasmon region of the energy-loss spectrum. Particularly in the presence of a strong plasmon signal (thick specimen), the proximity may introduce considerable error in quantifying the Mg concentration. Therefore, we recorded elemental maps only in very thin specimen regions ($<0.4\,\lambda \approx 60$ nm, where $\lambda \approx 140$ nm is the mean free path length of inelastic scattering [27, 28]).

XEDS is enabled on our instrument by an X-ray energy-dispersive spectrometer (EDAX^{TM}) with a selected Si–Li detector (energy resolution better than 130 eV at Mn-$K_{\alpha 1}$). XEDS line scans were conducted in STEM mode, based on Z-contrast imaging with the aid of a HAADF detector (Model 3000, Fischione Instruments). The FWHM of the electron probe we employed for XEDS line scans was ≈0.5 nm, corresponding to gun lens setting # 7 and spot size # 6 in nano-probe mode. The foil thickness in the regions in which we recorded XEDS line scans was below $1.5\lambda \approx 200$ nm. For this thickness, a single-scattering model predicts a resolution limit of 7.7 nm [27, 29]. Under our experimental conditions, the true resolution seems to be significantly better—likely because of channeling [30], although for the sake of accurate quantification we tried to minimize channeling by tilting away from low-indexed zone axes.

Cross-sectional specimens for TEM were prepared using standard methods, including mechanical preparation, dimple grinding down to a residual thickness of about 15 μm, and Ar^+ ion-beam thinning to electron transparency in a precision ion polishing system (PIPS, Gatan Inc.).

Table 1 Experimental conditions for the acquisition of the elemental maps

Element	Edge onset (eV)	Pre-edge 1 (eV)	Pre-edge 2 (eV)	Post-edge (eV)	Window (eV)	Acq. time (s)
Mg-L	51	38	46	55	8	3
Al-L	73	56	66	78	10	3
O-K	532	484	514	547	30	30

Results

As-grown Interfaces

Figure 2a shows the typical morphology and atomistic structure of the Al–$MgAl_2O_4$ interface as grown by MBE. The dark features in the Al are line defects and point defect agglomerates, most likely introduced during TEM specimen preparation or by electron beam damaging during observation, rather than during MBE growth. As expected and confirmed by electron diffraction, the aluminum layer is free of large-angle grain boundaries and has grown in ''cube-on-cube'' orientation relationship with the $MgAl_2O_4$ substrate:

$$\langle 100\rangle_{Al} \| \langle 100\rangle_{MgAl_2O_4}, \tag{6}$$

$$\{001\}_{Al} \| \{001\}_{MgAl_2O_4}. \tag{7}$$

The Al–$MgAl_2O_4$ interface is parallel to the planes (7).

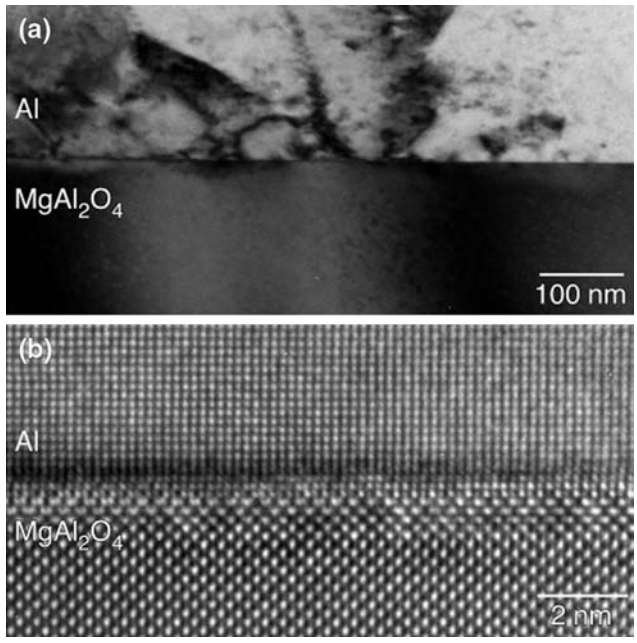

Fig. 2 (**a**) Cross-sectional TEM bright-field image of an as-grown Al–$MgAl_2O_4$ interface made by MBE. (**b**) HRTEM image of the interface in (**a**). The dark and bright Fresnel fringes along the Al–$MgAl_2O_4$ interface are artifacts of HRTEM imaging

The atomistic structure, revealed in Fig. 2b, closely resembles the structure we observed in previous work [19, 20]. In particular, the transition form the crystal structure of $MgAl_2O_4$ to the crystal structure of Al occurs within the thickness of one atom layer.

Figure 3 presents a zero-energy-loss-filtered image (ZL) of the interface in Fig. 2, elemental maps of Al, Mg, and O obtained by the three-window method, and an XEDS line scan across the interface. The elemental maps as well as the XEDS line scan confirm that the interface between the metal and the oxide is ''sharp,'' i.e. constitutes an abrupt transition in structure and composition. In particular, the Mg and the oxygen map do not show significant intensity on the metal side of the interface. In the XEDS line scan at the bottom of Fig. 3, the metal–oxide interface is at $x_i \approx 48$ nm. The finite width of the transition region of all three elemental profiles, estimated to ≈3 nm, is exclusively attributed to the non-negligible diameter of the electron probe and the inevitable effect of beam broadening in the specimen. The levels of Mg, Al, and oxygen measured in the $MgAl_2O_4$ reflect the stoichiometry, except that the measured Mg level exceedes the true level by a factor ≈ 1.3. The fluctuations in the concentrations observed in the $MgAl_2O_4$ far away from the Al–$MgAl_2O_4$ interface indicate absolute reliabilities of ± 1%, ± 2%, and ± 2% for X_{Mg}, X_{Al}, and X_O, the atom fractions of Mg, Al, and oxygen, respectively.

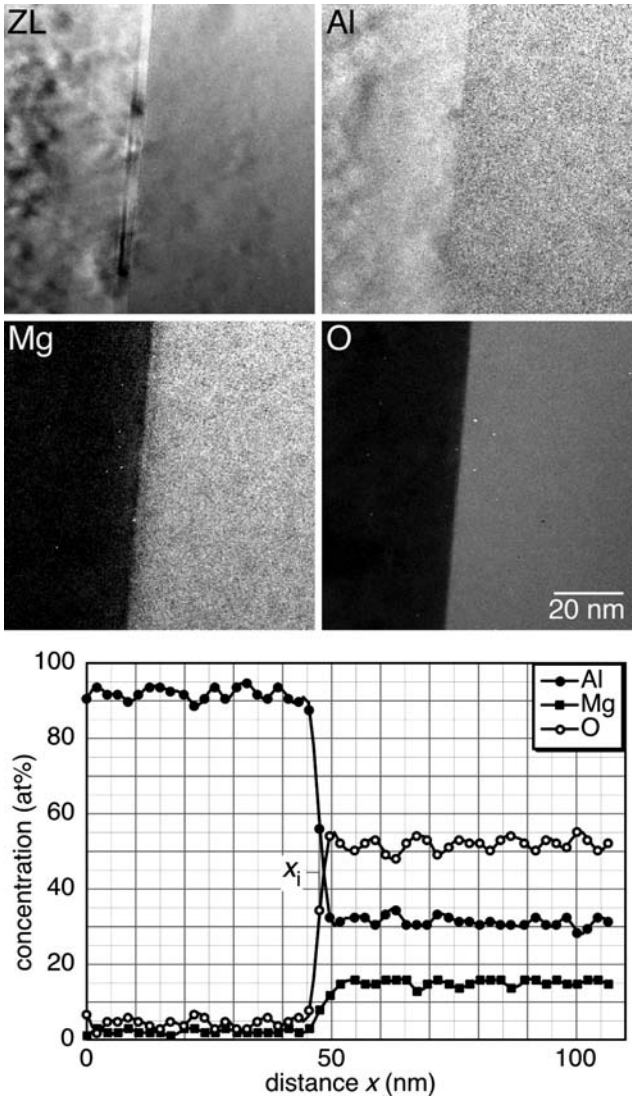

Fig. 3 Zero-loss-filtered image (ZL), elemental maps of Mg, Al, and oxygen, and XEDS line scan across the interface shown in Fig.2, an Al–$MgAl_2O_4$ interface ''as grown'' by MBE. In the elemental maps, the metal is on the left, the oxide on the right

Plain annealing—without applied electric field

Figure 4 shows the structure of the MBE-grown interface after plain annealing (without applied electric field) for 10 h at 893 K in UHV. In the CTEM image, Fig. 4a, no significant difference is observed compared to Fig. 2a. The main contrast features at the Al–$MgAl_2O_4$ interface are dark lines on the Al side, which we interpret as strain contours arising from the (very small) lattice misfit between bulk Al and $MgAl_2O_4$. Confirming the structural similarity with the specimen in the as-grown condition, the high-resolution image of Fig. 4b does not indicate any obvious structural change compared to Fig. 2b.

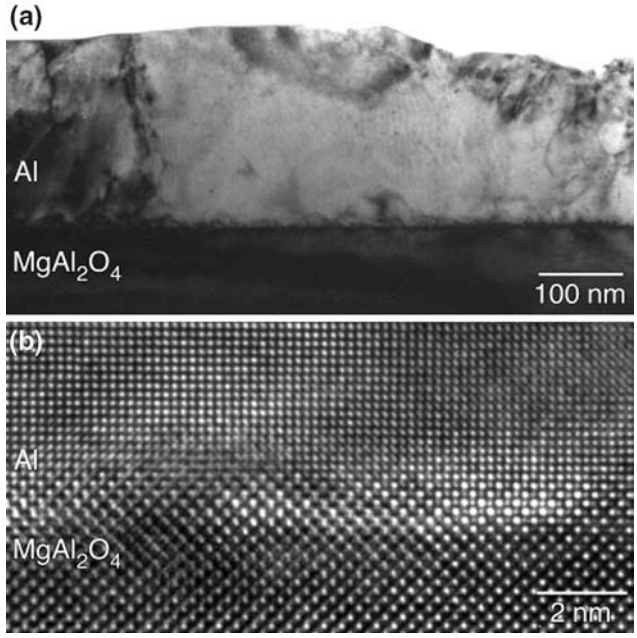

Fig. 4 (**a**) Cross-sectional TEM bright-field image of an MBE-grown Al–$MgAl_2O_4$ interface after plain annealing for 10 h at 893 K (without applied electric field). (**b**) HRTEM image of the interface in (**a**)

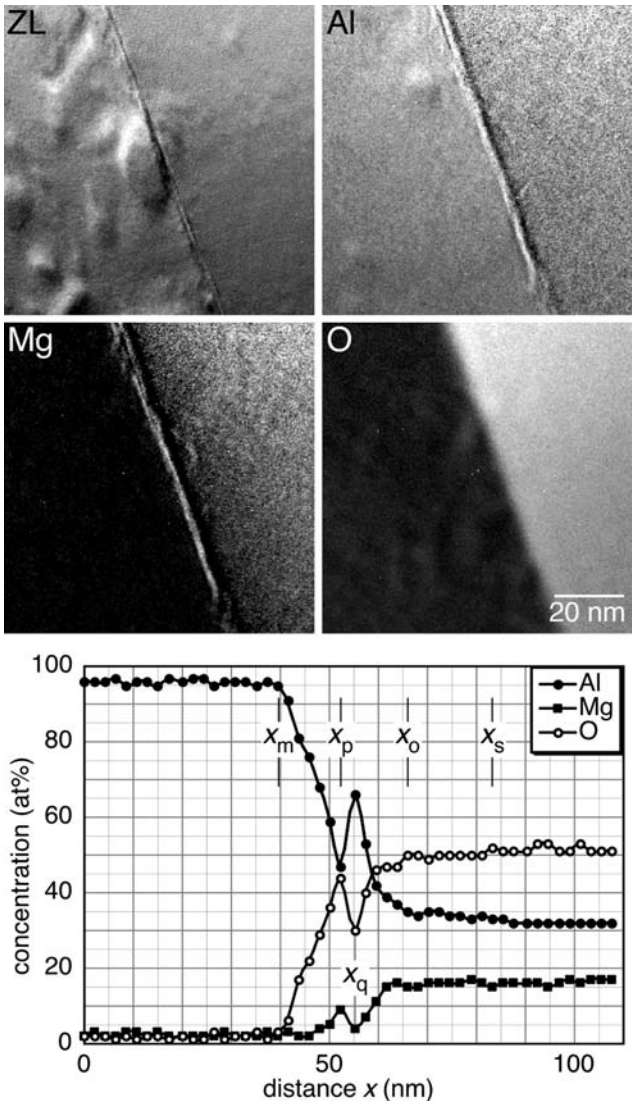

Fig. 5 Zero-loss-filtered image (ZL), elemental maps of Mg, Al, and oxygen, and XEDS line scan across the interface shown in Fig.4, which was obtained after plain annealing for 10 h at 893 K (without applied electric field). In the elemental maps, the metal is in the lower left, the oxide in the upper right

The analytical data in Fig. 5, in contrast, does reveal a significant effect of the annealing treatment. In contrast to the sharp transition in structure, the elemental maps and the XEDS line scan in Fig. 5 indicate that the compositional profiles of all three elements have substantially broadened by interdiffusion. Different from the XEDS line scan in Fig. 3, where the transition of the atomic fractions X_{Mg}, X_{Al}, and X_O occurs over a region of ≈3 nm, the corresponding transition widths in Fig. 5 are ≈45 nm for X_{Al}, ≈45 nm for X_O, and ≈20 nm for X_{Mg}. Approaching the metal–oxide interface from the metal side (left), X_{Al} begins to decay at $x_m \approx 40$ nm. Approaching the interface from the oxide side (right), a notable deviation from the plateaus representing the concentrations of the three elements in stoichiometric $MgAl_2O_4$ begins at $x_s \approx 84$ nm. Between x_m and x_s, at $x_p \approx 52$ nm, the XEDS line scan and the ESI maps consistently indicate a 3 nm wide local maximum of X_{Mg} and X_O, whereas X_{Al} features a corresponding minimum. At $x_q \approx 55$ nm, in contrast, the X_{Mg} and X_O exhibit a local minimum, while X_{Al} goes through a maximum. This phenomenon and the related "spikes" in the concentration profiles $X_{Mg}[x]$ and $X_{Al}[x]$ were observed in some, but not all TEM specimens we prepared after plain annealing. In the region between $x_q \approx 77$ nm and x_s, the Al concentration profile $X_{Al}[x]$ has the shape of an error-function, typically encountered for diffusion from a semi-infinite source. X_{Mg} and X_O are correspondingly lower in this region, and the concentration profiles $X_{Mg}[x]$ and $X_O[x]$ exhibit a shape resembling what one would expect for outward diffusion of Mg and oxygen from the oxide into the metal.

Annealing in the presence of an applied electric field—Al positive

Figure 6 reveals the typical result of applying a voltage $U_a = +125$ V for 10 h at 893 K in UHV. The CTEM image, Fig. 6a, features a distinct reaction layer

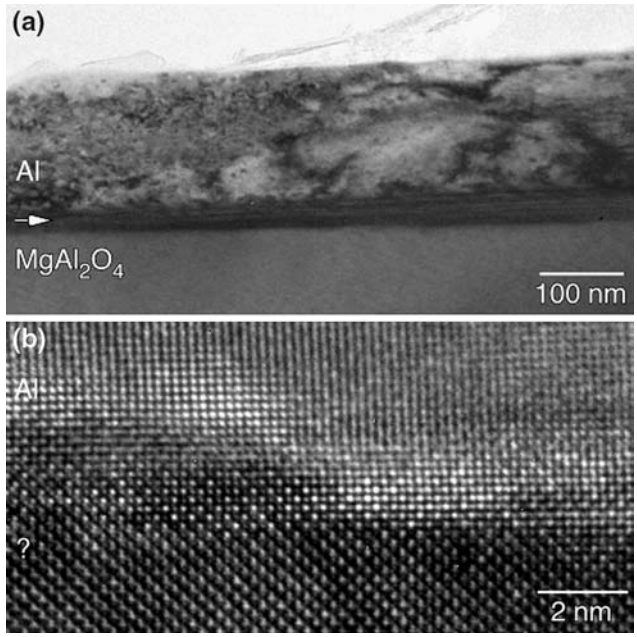

Fig. 6 (**a**) Cross-sectional TEM bright-field image of an MBE-grown Al–$MgAl_2O_4$ interface after annealing for 10 h at 893 K while applying a voltage of $U_a = +125$ V across the 250 μm thick spinel substrate. Note the dark layer between the $MgAl_2O_4$ substrate and the Al layer (arrow). (**b**) HRTEM image of the interface in (**a**)

between the Al layer and the $MgAl_2O_4$ substrate. The thickness of the layer ranges between 5 nm and 10 nm, and the interfaces it makes with the Al above and the $MgAl_2O_4$ below both appear like sharp phase boundaries. The HRTEM image in Fig. 6b zooms in on the interface between the reaction layer and the Al layer on top. In this image, the contrast pattern of the reaction layer resembles that of the spinel in Figs. 2b and 4b. While the interface between the reaction layer and the Al layer appears somewhat rougher than the Al-$MgAl_2O_4$ interface in Figs. 2b and 4b, the transition in structure seems to be equally abrupt: The contrast pattern in the HRTEM image changes over a distance corresponding to the thickness of only one or two monolayers.

Figure 7 presents the data we have obtained from the same specimen by analytical TEM. The oxygen map obtained by ESI and the oxygen concentration profile obtained by an XEDS line scan consistently reveal a constant (spatially homogeneous) and very small oxygen level X_O on the metal side and a high and equally constant X_O on the oxide side. According to the XEDS line profile, the oxygen concentration abruptly jumps from $X_O \approx 0$ on the metal side to $X_O \approx 0.40$ on the oxide side. The latter is very close to the expected value $X_O = 4/7$ for stoichiometric $MgAl_2O_4$, and the transition between the regions of different X_O at $x_i = 58$ nm is as sharp as it is for the as-grown material in Fig. 3. On the metal side, $x > x_i$, $X_{Mg} \approx X_O \approx 0$. On the oxide side, X_{Mg} and X_{Al} are constant for $x > x_s \approx 86$ nm. The average measured Mg level in this region is at $X_{Mg} \approx 0.14$, as expected for stoichiometric $MgAl_2O_4$. The average measured Al level is $X_{Al} \approx 0.32$, overestimating the true concentration by a factor of $f_{Al}^{-1} = 1.14$, whereas the measured level of oxygen is at $X_O \approx 55$, underestimating the true concentration by a factor $f_O = 1.04$.

In the region x_i, which has a width of ≈30 nm, X_{Al} smoothly increases from $X_{Al}[x_s] \approx 0.32$ to $X_{Al}[x_i] \approx 0.40$, while X_{Mg} decreases from $X_{Mg}[x_s] \approx 0.14$ to $X_{Mg}[x_i] \approx 0$. The concentration profiles $X_{Al}[x]$ and $X_{Mg}[x]$ are complementary ($X_{Al} + X_{Mg} \approx 1 - X_O$). $X_{Al}[x]$ roughly resembles an error function, as expected for inward diffusion of Al from a semi-infinite source, while $X_{Mg}[x]$ roughly corresponds to what one would expect for outward diffusion of Mg. However, plateaus are observed in both concentration profiles in the region x_i (arrowed in Fig. 7). Here, $X_{Al} \approx 0.38$, $X_O \approx 0.55$, while $X_{Mg} < 0.05$. Taking into account the slight errors in the measured levels of Al and oxygen, implying a correction factor $f_{Al}/f_O = 0.84$ for the X_{Al}/X_O ratio, this region consists of Al_2O_3 rather than $MgAl_2O_4$. The width of the plateau region, $|x_r - x_i| \approx 13$ nm, corresponds to the width of the reaction layer observed in Fig. 6a. The coherence of lattice planes across this layer observed in the HRTEM image of Fig. 6b suggests that the layer consists of γ-Al_2O_3, which is cubic with a face-centered cubic oxygen substructure and a lattice parameter very similar to that of $MgAl_2O_4$. The Mg-depleted region is also observed in the ESI map of Mg in Fig. 7, followed by a transition region in which the intensity steadily decreases towards the metal side. (The fine bright line at the position corresponding to x_i in the XEDS line profile is apparently an artifact.) In the ESI map of Al, the corresponding plateau of $X_{Al}[x]$ is less obvious,

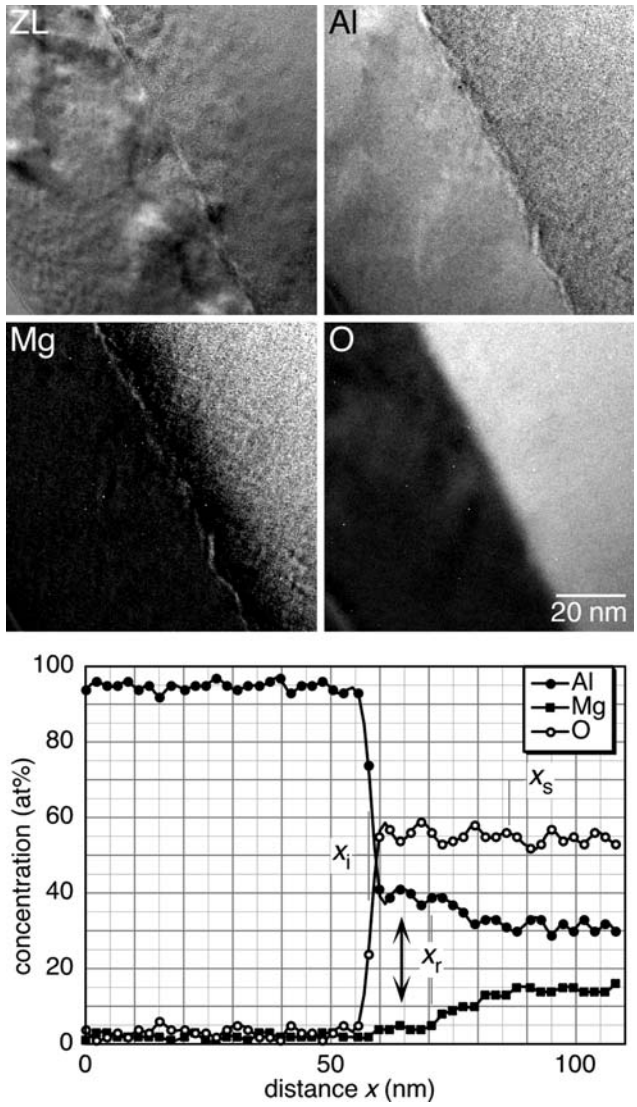

Fig. 7 Zero-loss-filtered image (ZL), elemental maps of Mg, Al, and oxygen, and XEDS line scan across the interface shown in Fig. 6, which was obtained after annealing for 10 h at 893 K while applying a voltage of U_a = + 125 V. In all elemental maps, the metal is in the lower left, the oxide in the upper right

presumably because the *relative* variation in the Al concentration is smaller than for Mg.

Figure 8 presents the results from an XEDS line scan obtained after annealing for 20 h at T_a = 893 K with U_a = + 125 V, i.e. after doubling the annealing time. Compared to the concentration profiles obtained after 10 h (Fig. 7), the plateau region x_i of $X_{Mg}[x]$ and $X_{Al}[x]$ has now broadened to $|x_r - x_i| \approx 120$ nm. All other features of the composition profiles, including the near-Al_2O_3 composition of the plateau region (arrowed), correspond to those observed in Fig. 7.

Annealing in the presence of an applied electric field—Al negative

Figures 9 and 10 show the corresponding results of applying a voltage $U_a = -125$ V for 10 h at 793 K. Different from Fig. 6a, the TEM image in Fig. 9a does not expose a reaction layer. Closely resembling the as-grown Al–$MgAl_2O_4$ interface in Fig. 2, the images exclusively feature an interface between Al and $MgAl_2O_4$, and similar to the as-grown state, the interface appears to be atomically sharp and flat. The HRTEM image in Fig. 9b confirms an abrupt structural transition between Al and $MgAl_2O_4$—within a distance corresponding to the thickness of one or two monolayers. The corresponding elemental maps obtained by ESI are shown in Fig. 10. The maps suggest a relatively sharp step in the composition of all three elements at the metal–oxide interface. According to the XEDS line scan in Fig. 10, all three composition profiles are somewhat flatter than in the as-grown state (Fig. 3), but definitely sharper than the profiles observed across the reaction layer that formed at U_a = +125 V. In Fig. 10, the zone $x_{xm} < x < x_s$ where notable deviations occur from the respective concentrations in Al and $MgAl_2O_4$ has a width of only ≈13 nm.

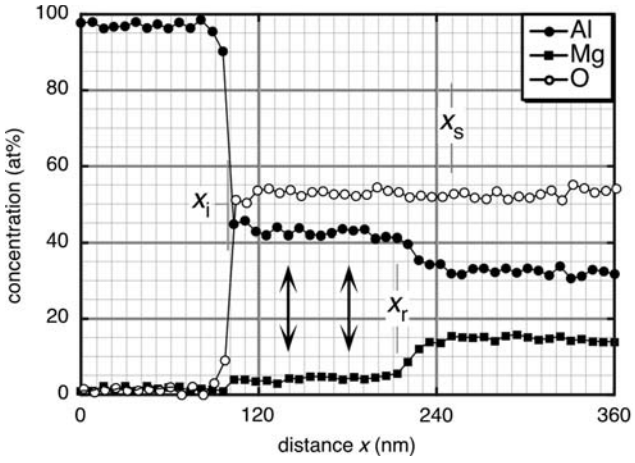

Fig. 8 XEDS line scan obtained after annealing for 20 h at 893 K while applying a voltage of U_a = +125 V

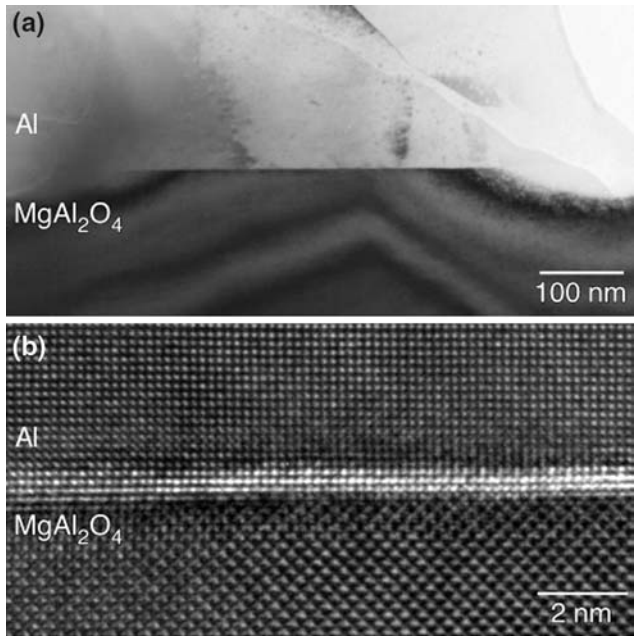

Fig. 9 (**a**) Cross-sectional TEM bright-field image of an MBE-grown Al–$MgAl_2O_4$ interface after annealing for 10 h at 893 K while applying a voltage of $U_a = -125$ V across the 250 μm thick spinel substrate. (**b**) HRTEM image of the interface in (**a**). The central bright fringe along the Al–$MgAl_2O_4$, accompanied by parallel dark fringes at the top and the bottom, is an artifact of HRTEM imaging

Discussion

The results of our studies consistently lead to the following conclusions:

(1) The Al–$MgAl_2O_4$ interface is not thermodynamically stable. On annealing, a diffusion reaction occurs that leads to considerable spatial redistribution of atomic species.

(2) Plain annealing (without applied electric field) broadens the initially sharp steps in the concentration profiles of Mg and Al and—apparently—also oxygen. The $MgAl_2O_4$ adjacent to the metal–oxide interface becomes deficient in Mg and richer in Al.

(3) Annealing $U_a = +125$ V accelerates the rate of Mg depletion and Al enrichment, while annealing with $U_a = -125$ V has the opposite effect, i.e. retards the re-distribution of Mg and Al.

(4) After all three types of annealing treatments, i.e. with $U_a = 0$ V, +125 V, and –125 V, the crystal structure of the oxide remains face-centered

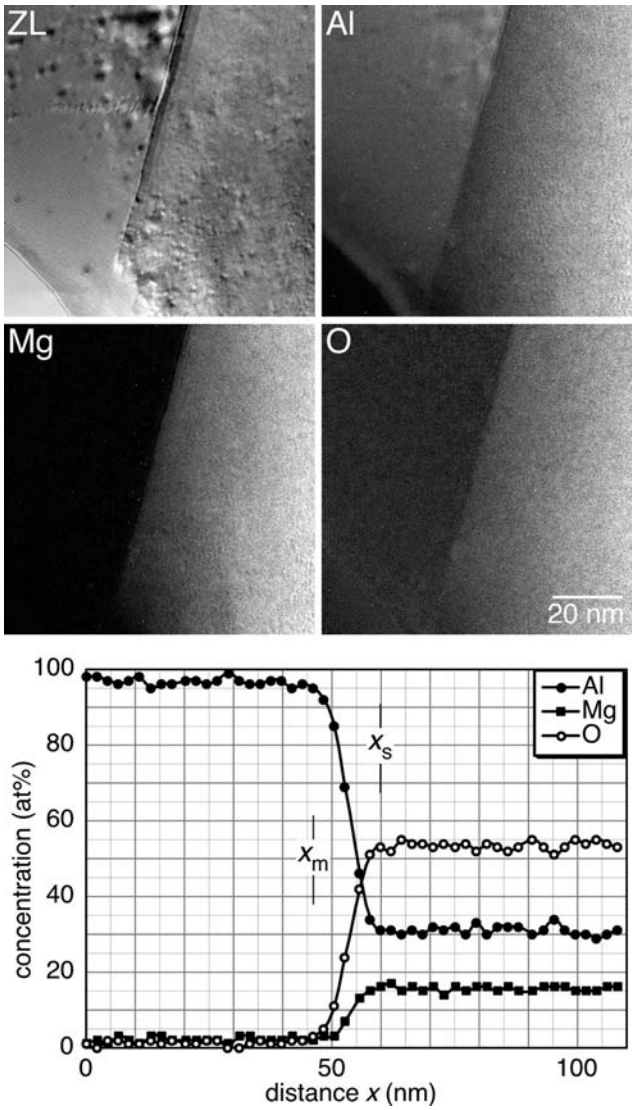

Fig. 10 Zero-loss-filtered image (ZL), elemental maps of Mg, Al, and oxygen, and XEDS line scan across the interface shown in Fig. 9, which was obtained after annealing for 10 h at 893 K while applying a voltage of $U_a = -125$ V. In the elemental maps, the metal is in the upper left, the oxide in the lower right

cubic, and the orientation relationship between the Al and the oxide remains ''cube-on-cube.''

The location of the structural interface observed in the HRTEM images cannot be directly correlated with the position of features in the ESI elemental maps and the XEDS line scans. This raises the question where the structural interfaces observed in the conventional and HRTEM images are located in the elemental maps and in the XEDS line scans. This question is particularly interesting for the rather complex composition profiles observed after plain annealing (Figs. 4b and 5). Recalling that the mobility of oxygen in spinel is small at T_a = 893 K and oxygen is nearly perfectly insoluble in Al [31], it seems possible that the observed broadening of the concentration profiles is an artifact, e.g. caused by beam broadening. However, all XEDS line scans were recorded under very similar conditions—particularly with respect to the local foil thickness. If beam broadening was the reason for the large width of the transition region $x_m < x < x_s$ in Fig. 5, the concentration profiles in Fig. 2 should show a comparable degree of convolution. However, they do not. Further, the sharpness of the ''spikes'' observed at x_p and x_q in Fig. 5, which may indeed be an artifact, demonstrate that the spatial resolution is in fact close to 3 nm, which corresponds well to the spatial resolution observed in Fig. 3 (assuming an ideally ''sharp'' interface).

If the observed width of the transition region is not an artifact, we must conclude that most of this region is not single phase: Stoichiometric spinel, $MgAl_2O_4$, can formally be written as $MgO \cdot n\,Al_2O_3$ with $n = 1$. According to the (quasi-binary) $MgO–Al_2O_3$ phase diagram, spinel can accommodate large deviations from the stoichiometric composition $MgAl_2O_4$, corresponding to $0.7 \le n \le 7.8$. Even for the most oxygen-deficient spinel, however, $X_O > 0.56$. Since the spinel in our experiments was stoichiometric ($n = 1$), the $X_O[x]$ should approach $X_O[n = 1] = 0.57$ in the region $x > x_s$ in Fig. 5—far away from the metal–oxide interface. However, the measured oxygen level in this region is only ≈ 0.52. Accordingly, the measurements underestimate the true oxygen concentration by a factor $f_O = 1.10$. But even after correcting for this deviation (assuming a linear relationship between measured and true X_O), only the region $x > x_o$ contains enough oxygen to consist entirely of spinel.

In the region $x_q < x < x_o$, where the deficiency of oxygen is significant, the reaction has either roughened the metal–oxide interface, generating islands of oxide with thin layers of metal between them, or decomposed the spinel to generate regions of Al-rich, metallic Al–Mg solid solution. Presumably, the alternating regions of metal and oxide are small and have their crystal lattices oriented parallel to each other. They will be difficult to detect in conventional and HRTEM images like Fig. 4 because the lattice mismatch between Al and the face-centered cubic oxygen substructure of spinel is very small [19, 20].

Although the solubility of oxygen in Al at $T_a = 893$ K is negligibly small, Fig. 5 indicates substantial oxygen levels between x_m and x_i on the metal side of the interface. Similar to the observations on the spinel side, this leads to the conclusion that this region contains γ-Al_2O_3 particles dispersed in the metal

matrix, which apparently do not generate sufficient contrast to be detected in Fig. 4. Again, this is possible because γ-Al_2O_3 has a face-centered cubic oxygen substructure with a negligible mismatch to the Al matrix, such that small γ-Al_2O_3 particles can make perfectly coherent, practically stress-free interfaces with the Al matrix. In the region around x_p, where Fig. 5 exhibits local maxima of X_{Mg} and X_O and a local minimum of X_{Al}, a considerable amount of oxygen seems to be bound in $MgAl_2O_4$ particles. This hypothesis is in agreement with the isothermal section of the Mg–Al–O phase diagram calculated for 1348 K [32]. For the measured composition of $Mg_{0.10}Al_{0.45}O_{0.45}$, the diagram predicts the coexistence of Al_2O_3 and $MgAl_2O_4$ in equilibrium with Al–Mg solid solution. Small particles of $MgAl_2O_4$ included in Al–Mg will again not be detectable under the imaging conditions of Fig. 4, either, owing to the similarity of the $MgAl_2O_4$ lattice parameter to those of Al and γ-Al_2O_3 and because it is highly likely that the crystal lattices of all three phases are oriented parallel to each other. However, the microscopic mechanism by which such microstructure can evolve demands further investigation.

Several features of the scenario observed in Figs.4 and 5 agree with the proposed ion exchange reaction (1). Most of all, the spinel adjacent to the metal–oxide interface $(x_o < x < x_s)$ features an Al composition profile indicating inward diffusion of aluminum and—although less pronounced—outward diffusion of Mg. In addition, the composition parameter n of the spinel in this zone is smaller than 1, corresponding to $X_O < 4/7$. This indicates a trend for this region to eventually form Al_2O_3.

When a voltage is applied across the $MgAl_2O_4$ layer, the resulting electrical field $\boldsymbol{E}_a$ does not penetrate the interior of the Al layer. Further, diffusion of Al atoms into spinel or ions from the spinel into the metal does not involve charge transport across the metal–oxide interface. Therefore, the main impact of the applied electric field will be to change the diffusion rates and spatial distribution of charged point defects in the spinel. The diffusion rate of charged point defects, in particular, changes because the electric field changes the activation energy of diffusion from Q to $Q - q\boldsymbol{E}_a \cdot \boldsymbol{r}$, where q is the charge of the point defect and $\boldsymbol{r}$ the jump vector.

As observed in the XEDS line scan of Fig. 7, the electric field generated by $U_a = +125$ V has a profound impact on the spatial distribution of Mg and Al. However, it does not significantly alter the distribution of oxygen. Very similar to the as-grown state (Fig. 3), Fig. 7 indicates $X_O[x<x_i] \approx 0$, $X_O[x>x_i] \approx 0.55$. This implies that x_i corresponds to the position of the metal–oxide interface before annealing, and that practically no transport of oxygen has occurred during annealing with $U_a = +125$ V.

The cation concentration profiles $X_{Mg}[x]$ and $X_{Al}[x]$ differ from those observed in the as-grown state (Fig. 3) and after plain annealing (Fig. 5). Similar to the latter between x_q and x_s in Fig. 5, the shapes of $X_{Mg}[x]$ and $X_{Al}[x]$ in the region x_i in Fig. 7 correspond to what one would expect for inward diffusion of Al and outward diffusion of Mg. However, there are two important aspects in which the profiles in Fig. 7 differ from those in Fig. 5: (i) $X_O[x]$ is constant, and X_{Mg} and X_{Al} are complementary in the region $x > x_i : X_{Mg}[x] + X_{Al}[x] = 1 - X_O[x] = 0.45$. (ii) Al diffused somewhat deeper into the $MgAl_2O_4$, and much more Mg is removed in the corresponding region (arrow in Fig. 7). The width $|x_s - x_i| \approx 30$ nm of the reaction layer, over which X_{Al} decreases from its maximum $X_{Al}[x_i] \approx 0.42$ at the interface to the $MgAl_2O_4$ level $X_{Al}[x_s] \approx 0.33$ and X_{Mg} raises from $X_{Mg}[x_i] \approx 0$ to $X_{Mg}[x_s] \approx 0.33$, is much larger than the width $|x_s - x_o| \approx 14$ nm of the Al diffusion zone in undecomposed spinel in Fig. 5. Considering the low concentration of Mg in the reaction layer and its distinct contrast it the TEM images of Fig. 6 leads to the conclusion that this layer is an early stage of γ-Al_2O_3 forming at the Al–$MgAl_2O_4$. Indeed, the layer broadens on prolonged annealing with $U_a = +125$ V and features a low and constant Mg concentration, as expected for γ-Al_2O_3 [27].

While annealing with $U_a = +125$ V promotes the diffusion of Al and Mg in the spinel, annealing with $U_a = -125$ V yields the opposite effect. The concentration profiles in Fig. 10 are very similar to those obtained from the as-grown material in Fig. 3. The main difference is that the transition from the composition of the metal to the composition characterizing stoichiometric $MgAl_2O_4$ occurs over a somewhat broader zone, namely between $x_m \approx 47$ nm and $x_s \approx 60$ nm. As discussed for the case $U_a = 0$ V, this region will include Al–Mg and γ-Al_2O_3.

Obviously, $U_a = +125$ V facilitates the exchange of Al ions for Mg ions in the $MgAl_2O_4$, while $U_a = -125$ V retards it. This observation agrees with the implication of the proposed ion exchange reaction (1), according to which the Al ions incorporated from the metal carry an effective charge of + 1. Consequently, the electric field generated by $U_a = +125$ V will drive the Al ions deeper into the $MgAl_2O_4$, which can explain why inward diffusion occurs to larger depth for this polarity of the applied voltage and less deep for the opposite voltage. Since ion exchange implies

dissolution of Mg in the Al layer, it also provides a high gain in configuration entropy. Based on these observations, it is very likely that the ion exchange reaction (1) actually does occur.

However, there is evidence that ion exchange is not the only operating micromechanism for Mg transport away from the Al–$MgAl_2O_4$. The alternative to be considered is transport of Mg ions into the opposite direction—away from the metal and deeper into the spinel. One piece of evidence supporting this hypothesis arises from the fact that we have not detected any Mg on the metal side of the interface—particularly not in Fig. 8, obtained after prolonged annealing (20 h) at T_a = 893 K with $U_a = +125$ V. Literature values for the pre-factor D_0 and the activation energy Q of the Mg diffusion coefficient in single-crystalline Al include $D_{0,Mg(Al)} = 6.23 \times 10^{-6}$ m^{-2}/s, $Q_{Mg(Al)} = 1.91 \times 10^{-19}$ J (1.19 eV) [33] and $D_{0,Mg(Al)} = 1.24 \times 10^{-4} m^{-2}/s$, $Q_{Mg(Al)} = 2.17 \times 10^{-19}$ J (1.35 eV) [34]. Accordingly, the mean diffusion distance $\sqrt{D_{Mg(Al)}t}$ of Mg after $t = 7.2 \times 10^4$ s is between 290 nm and 460 nm. Since this is comparable to the thickness of the Al layer, we may assume that dissolved Mg is distributed homogeneously in the Al layer. Approximating the true concentration profile $X_{Mg}[x]$ in Fig. 8 by $X_{Mg} = 0.04$ between x = 100 nm and x = 225 nm and $(X_{Mg}[x = 225\,nm] = 1/7)$ for $x >$ 225 nm, homogeneous distribution of all expelled Mg in the Al layer (thickness: 500 nm) would yield a Mg concentration of 3.7 at%. In Fig. 8, however, the Mg concentration in the region $x < x_i$ is clearly below this level.

The second reason why we believe that Mg from the oxide side of the Al–$MgAl_2O_4$ interface may also diffuse away from the Al metal originates from the observed behavior of the system under applied electric fields. During annealing with $U_a = +125$ V, the electric field across the interface not only promotes the migration of Al^{3+}, but also Mg^{2+} into the direction from Al to $MgAl_2O_4$. Therefore, the experimental observation that $U_a > 0$ accelerates the transport of Mg and $U_a < 0$ retards it not only supports the hypothesis of an ion exchange reaction, but is also consistent with Mg transport away from the metal.

Similarly, $X_{Mg}[x]$ agrees with the ion exchange mechanism, but also with the hypothesis of Mg transport towards the back-electrode. Provided that the mobility b_{Mg} of Mg in the spinel is higher than the b_{Al} of Al, the Mg concentration profiles on the spinel side in Figs. 5, 7, and 8 actually do not indicate outward diffusion of Mg, but can be explained as a consequence of rate-limiting inward diffusion of Al and the condition of charge neutrality, requiring that the X_{Mg} matches $X_O - X_{Al}$.

Finally, the ion exchange reaction (1) implies a redox reaction in which Al is oxidized and Mg is reduced. It appears that this is energetically unfavorable compared to a reaction in which Mg remains oxidized.

Figure 11 shows two corresponding models for Mg transport *away* from the metal, based on two different assumptions concerning the reaction products. In model A, $MgAl_2O_4$ decomposes into MgO and Al_2O_3 (without reducing Mg). This kind of ''kinetic'' decomposition is neither an oxidation nor a reduction and occurs when local differences of the chemical potential of oxygen μ_O exceed the critical value [35, 36]

$$\Delta\mu_{O,max} = \frac{2b_{Mg} + b_{Al}}{2b_{Mg} - 3b_{Al}} \Delta G^{\circ}_{MgAl_2O_4}. \quad (8)$$

Here, b denotes the ion mobility and $\Delta G^{\circ}_{MgAl_2O_4}$ the Gibbs free energy of formation of $MgAl_2O_4$ from MgO and Al_2O_3.

Since $b_{Mg} > b_{Al}$ in $MgAl_2O_4$ [37], MgO should form on the side of higher μ_O. For $U_a = +125$ V, this is the side of the Al back-electrode because of the applied electric field and because oxygen may be released e.g. from traps in the rough interface between the

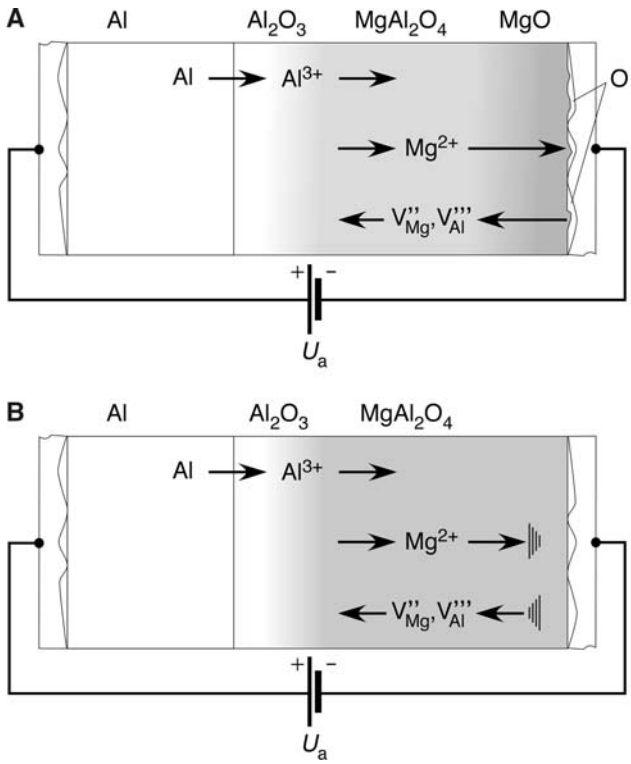

Fig. 11 Two models for reactions at the Al–$MgAl_2O_4$ interface based on Mg transport away from the metal

back-electrode (Al foil) or from the native oxide on the back-electrode. Absent additional sources of oxygen, the behavior of the back-electrode during annealing with $U_a = +125$ V should be equivalent to the behavior of the MBE-grown Al–$MgAl_2O_4$ interface during annealing with $U_a = -125$ V. However, there is a marked asymmetry with respect to inverting the polarity of the voltage, supporting the hypothesis that the back-electrode can provide additional oxygen [27].

The overall reaction corresponds to anodic oxidation of Al, involving the anode reaction

$$\mathrm{Al(ss)} \longrightarrow \mathrm{Al}_{\mathrm{Mg}}^{\bullet} + \mathrm{e}' \tag{9}$$

and the cathode reactions

$$\frac{1}{2}\mathrm{O_2\,(g)} + 2\mathrm{e}' \longrightarrow \mathrm{O}_{\mathrm{O}}^{\times} + \mathrm{V}_{\mathrm{Mg}}'' \tag{10}$$

$$\frac{3}{2}\mathrm{O_2\,(g)} + 6\mathrm{e}' \longrightarrow 3\mathrm{O}_{\mathrm{O}}^{\times} + 2\mathrm{V}_{\mathrm{Al}}''' \tag{11}$$

$$2\mathrm{O_2(g)} + 8\mathrm{e}' + \mathrm{Mg}_{\mathrm{Mg}}^{\times} + 2\mathrm{Al}_{\mathrm{Al}}^{\times} \longrightarrow \mathrm{MgAl_2O_4} + \mathrm{V}_{\mathrm{Mg}}'' + 2\mathrm{V}_{\mathrm{Al}}'''. \tag{12}$$

The cation vacancies created at the cathode according to (10) and (11) migrate toward the Al–$MgAl_2O_4$ interface. There, they are filled by neighboring Mg ions, leaving new Mg vacancies behind (toward the interface), which are subsequently occupied by Al ions incorporated from the Al layer, oxidized according to (9).

To date, the hypothesis of MgO formation at the back-electrode has not been experimentally verified. To account for the possibility that no elemental oxygen is available at the back-electrode, model B in Fig. 11 assumes that the migration of cations is accommodated by entirely by local changes in the composition of the spinel and exchange in cation sites up to the limit indicated by the Mg–Al–O phase diagram. This reaction results in the formation of Al_2O_3 at the anode and Mg-rich spinel at the cathode. Model B, accordingly, is based on the tolerance of $MgAl_2O_4$ for accommodating a large concentration of charged point defects.

Model A implies an electric current, while model B does not. In principle, therefore, it should be possible to determine the dominant operating mechanism by measuring the electric current during the annealing experiment. However, the current measurements we performed to date are not conclusive because they suffer from considerable impact of uncontrolled effects [27]. To obtain meaningful measurements, the current experimental setup needs to be replaced with a more sophisticated one. Further potential routes to distinguish between the proposed models include (i) deposition of Al on both sides of a spinel substrate, (ii) deposition of a closed film of Pt or a Pt grid on the backside of the spinel substrate to be able to control the oxygen activity, and (iii) patterning of the Al layer to observe the Al–$MgAl_2O_4$–vacuum triple-junction line.

Conclusion

The interface between Al and $MgAl_2O_4$ is not stable. Annealing at elevated temperatures causes a diffusion reaction eventually leading to substantial spatial re-distribution of atomic species. The experimental observations confirm a strong tendency for Al to replace Mg in the $MgAl_2O_4$ adjacent to the Al–$MgAl_2O_4$. The reaction rate can be sensitively controlled by applying an electric field across the spinel. A field oriented in the direction from the metal to the oxide accelerates the reaction, while the field in the opposite direction retards it. The underlying micromechanism includes ion exchange at the Al–$MgAl_2O_4$, as hypothesized in earlier work. However, the main direction of Mg transport is away from the metal, deeper into the $MgAl_2O_4$. The circumstances under which this transport occurs deserve further investigation. Since each one of the proposed mechanisms involves charged point defects in the $MgAl_2O_4$, the diffusion reaction will impact the adhesion between the metal and the oxide—according to the image charge theory of metal–oxide adhesion. Our results demonstrate that annealing in electric fields can be effectively employed to control interface microstructures and properties.

Acknowledgements We acknowledge the National Science Foundation for supporting this work under contract numbers DMR-0208008, DMR-0432196, and DMR-0114134.

References

1. Raj R, Saha A, An L, Hasselman DPH, Ernst F (2002) Acta Mater 50:1165
2. Sickafus K, Wills J (1999) J Am Ceram Soc 82:3279
3. Kröger F, Vink H (1956) Solid state physics. Academic Press Inc., San Diege, CA, pp 307–435
4. Rühle M, Heuer AH, Evans AG, Ashby MF (eds) (1992) In Proceedings of an international symposium on metal–ceramic interfaces. Acta Metall, vol 40
5. Rühle M, Evans AG, Ashby MF, Hirth JP (eds) (1990) Metal-ceramic interfaces. Acta-scripta metallurgica proceedings series. Pergamon Press, Oxford

6. Rühle M, Baluffi RW, Fischmeister HF, Sass SL (eds) (1985) In Proceedings of the international conference on the structure and properties of internal interfaces. J de Phys C4, vol 46
7. Ernst F (1995) Mater Sci Eng R14:97
8. Howe JM (1993) Int Mat Rev 38:233
9. Howe JM (1993) Int Mater Rev 38:257
10. Stoneham AM, Tasker PW (1988) J Phys C5 49:99
11. Stoneham AM, Tasker PW (1987) Philos Mag B 55:237s
12. Stoneham AM, Tasker PW (1986) In Pask JA and Evans AG (eds) Ceramic microstructures '86, Materials science research, vol 21. Plenum Press, New York, pp 155–165
13. Stoneham AM, Tasker PW (1985) J Phys C 18:L543
14. Finnis MW (1991) Surface Sci 241:61
15. Finnis MW (1992) Acta Metall Mater 40:S25
16. Duffy D, Harding J, Stoneham A (1993) Phil Mag A 67:865
17. Duffy DM, Harding JH, Stoneham AM (1992) Acta Metall Mater 40:S11
18. Purton J, Parker SC, Bullett DW (1997) J Phys: Condens Matter 9:5709
19. Schweinfest R, Köstlmeier S, Ernst F, ElsÄsser C, Wagner T, Finnis MW (2001) Philos Magazine A (Physics of Condensed Matter: Structure, Defects and Mechanical Properties) 81:927
20. Schweinfest R, Ernst F, Wagner T, Rühle M (1999) J Microscopy 194:142
21. Fu Q, Wagner T (2005) Surface Sci 574:L29
22. Fu Q, Wagner T (2005) J Phys Chem 109:11697
23. Foxon CT (2003) J Crystal Growth 251:1
24. Schweinfest R, Ernst F, Wagner T, Rühle M (1999) J Microscopy 194:142
25. Schweinfest R (1998) Ph.D. thesis, Universität Stuttgart
26. Reimer L (1995) Energy-filtering transmission electron microscopy, Springer series in optical sciences, vol 71. Springer, Berlin
27. Yu Y (2005) PhD thesis, Case Western Reserve University
28. Egerton R (1996) Electron energy-loss spectroscopy in the electron microscope, 2nd edn. Plenum Press, New York
29. Reed S (1982) Ultramicroscopy 7:405
30. Chiang Y-M, Kingery W (1990) J Am Ceram Soc 73:1153
31. Taylor JR, Dinsdale AT, Hillert M, Selleby M (1992) Calphad: Comput Coupling Phase Diagrams Thermochem 16:173
32. Wanabe M, Aswath PB (1996) Acta Mater 45:4067
33. Rothman S, Peterson N, Nowicki L, Robinson L (1974) Phys Status Solidi B 63:K29
34. Hirano K, Fujikawa S (1978) J Nuclear Mater 69/70:564
35. Schmalzried H (1995) Chemical kinetics of solids. VCH Verlagsgesellschaft mbH, Weinheim
36. Schmalzried H (1990) J Chem Soc: Faraday Trans 86:1273
37. Whitney W, Stubican V (1970) Am Ceram Soc Bull 49:388